Large fanout optical interconnects using thick holographic gratings and substrate wave propagation

M. R. Wang, G. J. Sonek, R. T. Chen, and T. Jannson

Substrate wave propagation and Bragg diffraction by multiplexed holographic gratings have been used to demonstrate a new 1-to-30 fanout optical interconnect having an overall diffraction efficiency of 87.8% at 514.5 nm and an individual channel efficiency of ~3.0 ± 0.8%. The device configuration utilizes the large multiplexing capability of dichromated gelatin polymer films and substrate total internal reflection to realize large channel fanouts within the plane of a soda-lime glass substrate. A simplified theoretical formulation is presented to treat the corresponding three-dimensional holographic diffraction problem in the Bragg regime for slanted phase gratings. Results are compared with experimentally measured quantities for singly exposed phase gratings in different polarization conditions and incident angle orientations. The limitations of using multiplexed holograms in multiplanar substrate interconnection applications are also discussed.

Key words: Optical interconnect, fanout, holographic grating, planar integration.

1. Introduction

The advantages of optical interconnection techniques, including the ability to achieve high data rates, large fanout densities, and a reduction in capacitive and inductive loading effects, have been enumerated by several authors.[1-3] The use of holographic optical elements for the interconnection of very large-scale integrated circuits has also been described.[4-6] More recently the concept of planar integration has emerged as a means of monolithically interconnecting large numbers of optical and electronic components.[7-11] By incorporating the principles of both diffractive and reflective optics, planar substrate integration can be used to optimize wafer-scale interconnects for speed, bandwidth, channel fanout, cross talk, and alignment/space constraints. It is furthermore compatible with existing device and process technologies including surface emission[12] and epitaxial film transfer techniques.[11]

Here we report on the development of an optical interconnect that uses thick holographic diffraction gratings and substrate wave propagation to achieve a 1-to-30 channel fanout with an angular channel separation of 2° and an overall efficiency of ~87.8% at a 514.5-nm wavelength. A set of highly multiplexed gratings is used to diffract an incident light beam that propagates in an underlying glass substrate at its angle of total internal reflection. After being diffracted the beams propagate along different directions by reflecting off, or bouncing between, the upper and lower planes of the substrate. The technique, which is limited only by the number, efficiencies, and interaction lengths of multiplexed holograms that are fabricated on an appropriate substrate, should find widespread use in interconnection schemes for optical signal processing and computing applications.

To determine the potential and limitations of the above technique, a detailed study of thick holographic dichromated gelatin (DCG) gratings on glass substrates has been carried out. A simplified theoretical analysis is presented for general three-dimensional (3-D) planar grating diffraction by single slanted transmission phase gratings in the Bragg regime. The results of this analysis are then compared with the experimental results from grating diffraction measurements taken in different polarization conditions and incident angle orientations. The experimental and theoretical results are found to be in good agreement

M. R. Wang, R. T. Chen, and T. Jannson are with the Physical Optics Corporation, 2545 West 237th Street, Torrance, California 90505. M. R. Wang and G. J. Sonek are with the Department of Electrical and Computer Engineering, University of California, Irvine, California 92717.

Received 10 October 1990
0003-6935/92/020236-14$05.00/0.

for all parametric cases considered. Finally, design considerations and experimental results for large fanout multiplexed holograms, which are used in conjunction with the substrate propagation technique, are presented. Interconnectivity issues and their dependence on fundamental material properties are also discussed.

II. Substrate Optical Interconnect Concept

The basic model for optical interconnection at the wafer-scale level, which uses multiplexed holograms and substrate wave propagation, is depicted in Fig. 1(a). Here the upper and lower planes of a suitable substrate constitute the planes between which optical elements are to be interconnected. The components, which include surface-emitting laser diodes and optical photodetectors, can conceivably be patterned on both sides of the substrate by using conventional lithographic, etching, and processing techniques[8] or more novel epitaxial techniques[13] when amorphous or noncrystalline materials are used.

As shown in Fig. 1(a) the holographic elements can serve any one of several functions, which include focusing, multiplexing, or beam collimation. Light that is launched into the substrate through a surface-emitting source, or that already propagates within the substrate as a substrate mode, can be diffracted into different directions on its encounter with a thick multiplexed transmission holographic grating when the Bragg diffraction condition is satisfied. We note that the use of a transmission hologram in this geometry as shown in Fig. 1(b) depends on the phenomenon of total internal reflection (TIR) at the polymer film–air interface. Compared with the reflection holograms, the light beam in this case is transmitted through the hologram, diffracted, reflected through TIR, and then diffracted again to produce the substrate mode holographic interconnect. Based on the interaction length and the magnitude of the grating wave vector, the multiplexed hologram either exhibits a single diffractive order in the Bragg regime or multiple diffractive orders. Once diffracted the beam continues to propagate through the substrate through multiple reflections between the upper and lower substrate planes until it exits the substrate or is subsequently diffracted by yet another holographic element. Fresnel losses at the air–substrate interfaces can be reduced by the application of suitable reflection coatings. This technique has the advantage of optimizing space on the wafer by replacing conventional planar metallic interconnects with high-density optical transmission channels that are defined within the substrate itself.

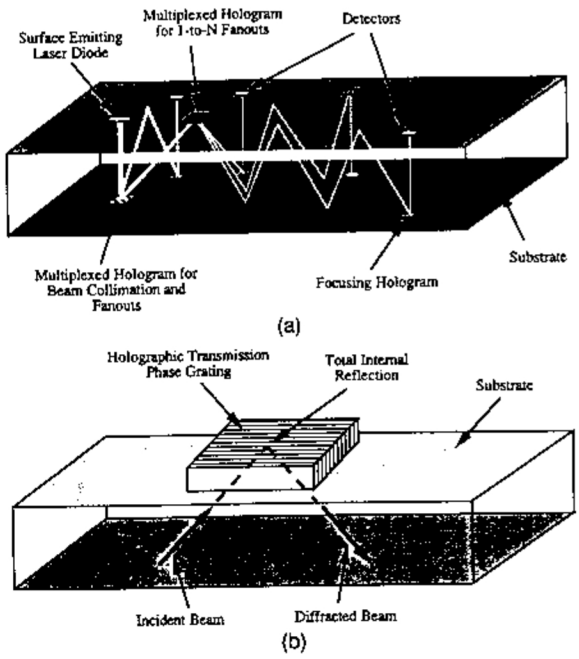

Fig. 1. (a) Optical interconnection scheme for achieving large fanout densities by using multiplexed holograms and substrate wave propagation. (b) Expanded view of the hologram–substrate interface. Bragg diffraction and TIR from an unslanted transmission grating are used in this case to construct a multiplexed hologram for 1-to-N fanouts.

We consider the use of DCG polymer films, coated and then processed on top of soda-lime glass substrates, to demonstrate the concept of large fanout planar substrate interconnects. The same concepts described here can similarly be applied to holographic and substrate materials other than DCG and glass as well, provided that substrate attenuation losses at the desired operating wavelength are minimized. In the present case DCG films are processed to produce only one Bragg diffracted beam per grating with diffraction angles in the plane of the substrate spaced uniformly from 30° to 88°, respectively. The substrate mode remains confined to the glass medium as long as its bounce angle exceeds ~41.8°, i.e., the critical angle for TIR at the air–glass interface.

III. Simplified Analysis of 3-D Holographic Grating Diffraction in the Bragg Regime

As described above the thick holographic grating performs the primary function of demultiplexing the input optical signal either by redirecting the incident substrate mode along a new path within the substrate plane or by coupling light into the substrate mode from the overlying grating region. The 3-D vector-coupled grating diffraction problem, in the case in which the grating is bounded by two different homogeneous media, has been examined.[14-16] However, a complete modal analysis often yields complicated results, because the grating vector can have an arbitrary orientation with respect to the plane of incidence. As a consequence the transverse electric (TE) and transverse magnetic (TM) incident field components become coupled inside the grating region and can no longer be treated separately as in the two-dimensional (2-D) case.[17]

The 3-D problem can be greatly simplified, however, if we recognize that in the Bragg regime a transformation plane can be identified that contains the incident, grating, and diffracted wave vectors $\mathbf{k}$, $\mathbf{K}$, and $\mathbf{k}_d$, respectively. The identification of such a

plane reduces the problem to a 2-D scalar formulation, which can then be solved by using conventional coupled-wave theory.[17]

The basic geometry for 3-D diffraction from a thick planar hologram that contains slanted phase gratings is shown in Fig. 2. Here ϕ defines the slant angle of a planar holographic phase grating and α defines the angle of incidence for a linearly polarized plane wave. The holographic grating of arbitrary orientation may be characterized by a periodic permittivity as

$$\epsilon(x, z) = \epsilon_0 + \epsilon_1 \cos(\mathbf{K} \cdot \mathbf{r}), \tag{1}$$

where ϵ_0 is the permittivity of the unmodulated region, ϵ_1 is the modulation amplitude, and $\mathbf{r}$ is a position vector in the (x, y, z) coordinate system. The index of refraction of this grating is then

$$n = [\epsilon(x, z)]^{1/2} \approx \sqrt{\epsilon_0} + \frac{1}{2}\frac{\epsilon_1}{\sqrt{\epsilon_0}} \cos(\mathbf{K} \cdot \mathbf{r}) \qquad \epsilon_1 \ll \epsilon_0 \tag{2a}$$

or

$$n = n_0 + \Delta n \cos(\mathbf{K} \cdot \mathbf{r}), \tag{2b}$$

where n_0 is the index of refraction of the unperturbed region and Δn is the amplitude of index modulation. Here it is assumed that the entire grating is surrounded by a uniform homogeneous medium of refractive index n_0. The Fresnel equations can, however, be used to treat the case in which several different homogeneous media surround the grating region. By using the coordinate system shown in Fig. 2, we can write the grating vector $\mathbf{K}$, which lies in the x–z plane, as

$$\mathbf{K} = K \sin\phi\hat{x} + K \cos\phi\hat{z}, \tag{3}$$

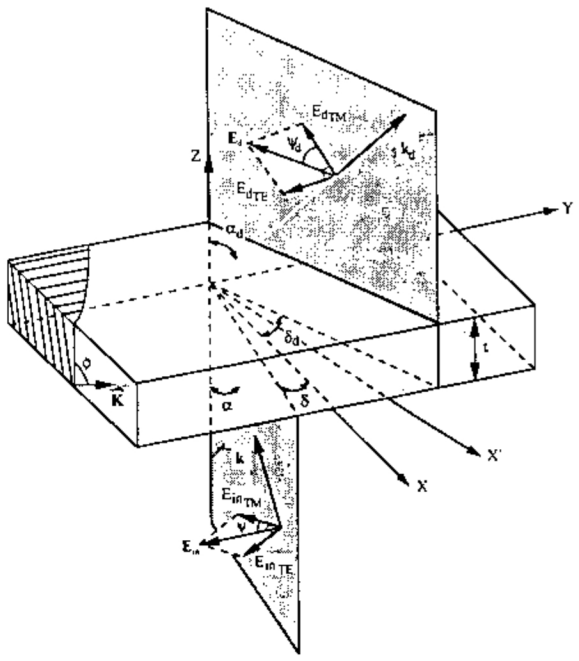

Fig. 2. Basic geometry for 3-D diffraction from a thick holographic slanted phase grating.

where $K = (2\pi)/\Lambda$, Λ is the grating period, and ϕ is the grating slant angle.

In this same coordinate system of Fig. 2 the incident plane-wave propagation vector $\mathbf{k}$ can be written as

$$\mathbf{k} = k_x\hat{x} + k_y\hat{y} + k_z\hat{z} \tag{4a}$$

or

$$\mathbf{k} = k_0 \sin\alpha \cos\delta\hat{x} + k_0 \sin\alpha \sin\delta\hat{y} + k_0 \cos\alpha\hat{z}, \tag{4b}$$

where k_0, equal to $[(2\pi)/\lambda]n_0$, is the propagation constant in the medium of index n_0, α is the angle of incidence, and δ is the angle between the plane of incidence and the x axis, which is defined as

$$\delta = \tan^{-1}\left(\frac{k_y}{k_x}\right). \tag{5}$$

Here both α and k_x are chosen to have the same sign. A general unit polarization vector can also be defined for the incident plane wave and is given by the expression

$$\hat{u} = u_x\hat{x} + u_y\hat{y} + u_z\hat{z}, \tag{6a}$$

with

$$\begin{aligned} u_x &= -\cos\psi \cos\alpha \cos\delta + \sin\psi \sin\delta, \\ u_y &= -\cos\psi \cos\alpha \sin\delta - \sin\psi \cos\delta, \\ u_z &= \cos\psi \sin\alpha, \end{aligned} \tag{6b}$$

where ψ is the polarization angle and assumes the values of 0° and 90° for incident TM- and TE-polarized waves, respectively.

We recall that, in the general 3-D diffraction problem, the TE and TM components cannot be decoupled.[14] However, in the Bragg regime the phase-matching condition requires that the incident, diffracted, and grating wave vectors, $\mathbf{k}$, $\mathbf{k}_d$, and $\mathbf{K}$, respectively, lie on a common plane, known as the diffraction plane, as shown in Fig. 3. By considering only a single diffracted order from an arbitrarily oriented phase grating with an oblique angle of incidence, we can use the scalar coupled-wave theory to treat separately the parallel ($\parallel$) and perpendicular ($\perp$) field components of the optical wave within this diffraction plane. Here the $\parallel$ field component lies in the diffraction plane, while the $\perp$ component lies along the vector $\mathbf{n}$ direction, which is normal to the diffraction plane, as shown in Fig. 3. The resultant electromagnetic field of the diffracted wave can then be obtained by the vector summation of these two components.

To facilitate the simplified formulation of the 3-D diffraction problem, a coordinate transformation from (x, y, z) to (x', y', z') is performed. The resultant diffraction plane is shown in Fig. 3. Because of the oblique angle of incidence, the effective grating interaction length is now d instead of the grating thickness t. The grating slant angle in the new coordinate system is ϕ', and the new incident angle is α', which is

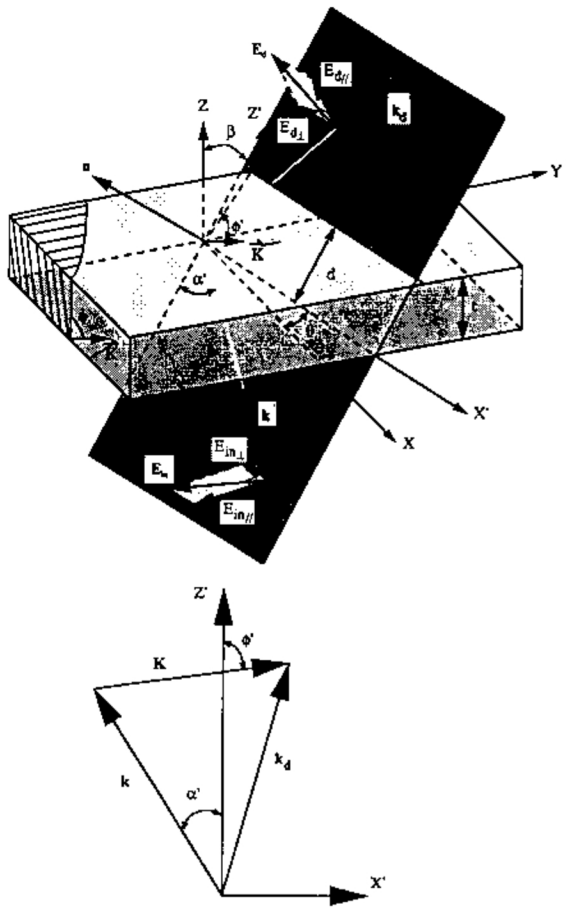

Fig. 3. Modified geometry for the Bragg diffraction problem. The rotated coordinate system (x', y', z') and a new transformation plane that contains the incident, diffracted, and grating wave vectors $\mathbf{k}$, $\mathbf{k}_d$, and $\mathbf{K}$, respectively, are shown. The phase-matching condition in the primed coordinate system is shown in the inset.

measured between $\mathbf{k}$ and the z' axis. The grating constant $\mathbf{K}$ satisfies the well-known phase-matching condition and is also shown in Fig. 3.

To obtain the coordinate rotation angles θ and β in Fig. 3, we first find the vector $\mathbf{n}$ that is normal to the diffraction plane. Hence

$$\mathbf{n} = \frac{\mathbf{K} \times \mathbf{k}}{k_0 K} = A_x\hat{x} + A_y\hat{y} + A_z\hat{z}, \tag{7}$$

where

$$\begin{aligned} A_x &= -\sin\alpha \sin\delta \cos\phi, \\ A_y &= \sin\alpha \cos\delta \cos\phi - \cos\alpha \sin\phi, \\ A_z &= \sin\alpha \sin\delta \sin\phi. \end{aligned} \tag{8}$$

The normalized unit vector $\hat{n}$ can be written as

$$\hat{n} = A_x'\hat{x} + A_y'\hat{y} + A_z'\hat{z}, \tag{9}$$

with

$$A_i' = A_i/(A_x^2 + A_y^2 + A_z^2)^{1/2} \tag{10}$$

and $i = x, y$, and z, respectively.

Therefore, the plane that passes through the origin with a normal vector $\hat{n}$, which corresponds to the diffraction plane, is defined by

$$A_x'x + A_y'y + A_z'z = 0. \tag{11}$$

The rotation of the coordinate axes from (x, y, z) to (x', y', z') is performed by first rotating counterclockwise around the z axis for angle θ and then rotating counterclockwise on the x' axis for angle β. Negative angles are used to characterize the clockwise rotations. The transformation matrix equation is then given by

$$\begin{pmatrix} x \\ y \\ z \end{pmatrix} = [\mathrm{M}] \begin{pmatrix} x' \\ y' \\ z' \end{pmatrix}, \tag{12}$$

where the rotation matrix [M] is expressed as

$$[\mathrm{M}] = \begin{pmatrix} \cos\theta & -\sin\theta\cos\beta & \sin\theta\sin\beta \\ \sin\theta & \cos\theta\cos\beta & -\cos\theta\sin\beta \\ 0 & \sin\beta & \cos\beta \end{pmatrix}. \tag{13}$$

The diffraction plane in the (x', y', z') coordinate system can now be described by the expression

$$\begin{aligned} &(A_x' \cos\theta + A_y' \sin\theta)x' \\ &\quad + (-A_x' \sin\theta \cos\beta + A_y' \cos\theta \cos\beta + A_z' \sin\beta)y' \\ &\quad + (A_x' \sin\theta \sin\beta - A_y' \cos\theta \sin\beta + A_z' \cos\beta)z' = 0. \end{aligned} \tag{14}$$

Since this diffraction plane is in fact the x'–z' plane, we have $y' = 0$, and the values for x' and z' on the plane can be arbitrarily chosen. This therefore requires that

$$A_x' \cos\theta + A_y' \sin\theta = 0, \tag{15}$$

$$A_x' \sin\theta \sin\beta - A_y' \cos\theta \sin\beta + A_z' \cos\beta = 0. \tag{16}$$

Hence

$$\tan\theta = -\frac{A_x'}{A_y'}, \tag{17}$$

$$\tan\beta = \frac{A_z'}{A_y' \cos\theta - A_x' \sin\theta}. \tag{18}$$

The effective grating interaction length d, as shown in Fig. 3, is now given by

$$d = \frac{t}{\cos\beta} = t\left(\frac{A_x'^2 + A_y'^2 + A_z'^2}{A_x'^2 + A_y'^2}\right)^{1/2}. \tag{19}$$

The transformation of the $\mathbf{K}$ vector into the (x', y', z') coordinate system gives

$$\mathbf{K} = K[(\sin\phi \cos\theta)\hat{x}' + (\sin\phi \sin\theta \sin\beta + \cos\phi \cos\beta)\hat{z}']. \tag{20}$$

The grating vector $\mathbf{K}$ also has a zero y' component since it lies within the diffraction plane. The grating

slant angle ϕ' in this x'–z' plane can therefore be obtained from the expression

$$\phi' = \tan^{-1}\left|\frac{K_{x'}}{K_{z'}}\right| = \tan^{-1}\left|\frac{\sin\phi\cos\theta}{\sin\phi\sin\theta\sin\beta + \cos\phi\cos\beta}\right| \tag{21}$$

Similarly, the transformation of the incident $\mathbf{k}$ vector yields

$$\mathbf{k} = k_{x'}\hat{x}' + k_{z'}\hat{z}', \tag{22a}$$

where

$$\begin{aligned} k_{x'} &= k_0[\sin\alpha\cos\delta\cos\theta - \sin\alpha\sin\delta\sin\theta\cos\beta \\ k_{z'} &= k_0[\sin\alpha\cos\delta\sin\theta\sin\beta - \sin\alpha\sin\delta\cos\theta\sin\beta \\ &\quad + \cos\alpha\cos\beta]. \end{aligned} \tag{22b}$$

Again, the zero y' component of $\mathbf{k}$ confirms its presence in the diffraction plane. The incident angle α', measured between $\mathbf{k}$ and the z' axis, is now given by

$$\alpha' = \tan^{-1}\left|\frac{k_{x'}}{k_{z'}}\right|, \tag{23}$$

where $k_{x'}$ and $k_{z'}$ are defined in Eqs. (22b).

Now that we have transformed the relevant parameters into the diffraction plane, the coupled-wave theory[17] can be applied by using the known values of α' and ϕ', the grating interaction length d, and the grating constant K to treat the in-plane Bragg diffraction problem for the $\parallel$ and $\perp$ field components, respectively.

The phase-matching conditions for the in-plane diffraction are obtained from the phase-matching diagram of Fig. 3 and are given by

$$k_{dx'} = k_{x'} \pm K\sin\phi', \tag{24}$$

$$k_{dz'} = k_{z'} \pm K\cos\phi', \tag{25}$$

where $\pm$ is used when $\phi' - \alpha' > 90°$ ($< 90°$), respectively.

Now let $k_d = (k_{dx'}^2 + k_{dz'}^2)^{1/2}$ be the propagation constant of the diffracted wave. When the Bragg condition is satisfied, we should have

$$k_d = k. \tag{26}$$

When the Bragg condition is not satisfied because of a slight angular or wavelength deviation, we may define a dephasing constant ϑ in analogy to the coupled-wave approach to characterize the off-Bragg condition diffraction behavior. Hence

$$\vartheta = \frac{k_{z'}^2 - k_{x'}^2}{2k_{z'}}. \tag{27}$$

The diffraction efficiencies η for $\perp$ and $\parallel$ polarized optical waves, with the consideration of diffraction caused by possible dephasing in a lossless grating, are given as follows[17]:

$$\eta_\perp = \frac{4\kappa^2}{\left(\frac{C_z}{C_d}\right)\vartheta^2 + 4\kappa^2}\sin^2\left[\frac{1}{2}\left|\frac{\vartheta^2}{C_d^2} + \frac{4\kappa^2}{C_z C_d}\right|^{1/2} d\right], \tag{28}$$

$$\eta_\parallel = \frac{4\kappa^2(\hat{k}\cdot\hat{k}_d)^2}{\left(\frac{C_z}{C_d}\right)\vartheta^2 + 4\kappa^2(\hat{k}\cdot\hat{k}_d)^2}\sin^2\left[\frac{1}{2}\left|\frac{\vartheta^2}{C_d^2} + \frac{4\kappa^2(\hat{k}\cdot\hat{k}_d)^2}{C_z C_d}\right|^{1/2} d\right], \tag{29}$$

where

$$C_z = \frac{k_{z'}}{k_0}, \tag{30}$$

$$C_d = \frac{k_{dz'}}{k_d}, \tag{31}$$

$$\kappa = \frac{\pi\Delta n}{\lambda}. \tag{32}$$

Here $\hat{k}$ and $\hat{k}_d$ are unit vectors for the incident and diffracted wave propagation constants, and the z' subscripts indicate the z' components, respectively. For the off-Bragg condition, $k_0 \neq k_d$, and ϑ is used to characterize the dephasing of the coupling.

The incident $\perp$ field amplitude can be obtained by taking the projection of $\mathbf{E}_{in}$ along the direction of the vector $\mathbf{n}$. Hence

$$E_{in_\perp} = E_{in}U_\perp, \tag{33}$$

where

$$U_\perp = \hat{u}\cdot\hat{n} = u_{x'}A_{x'} + u_{y'}A_{y'} + u_{z'}A_{z'}. \tag{34}$$

Similarly, the incident $\parallel$ field amplitude is given by the projection of $\mathbf{E}_{in}$ along the $\hat{n}\times\hat{k}$ direction. Since

$$\hat{n}\times\hat{k} = B_x\hat{x} + B_y\hat{y} + B_z\hat{z}, \tag{35a}$$

where

$$\begin{aligned} B_x &= A_{x'}\cos\alpha - A_{z'}\sin\alpha\sin\delta, \\ B_y &= A_{z'}\sin\alpha\cos\delta - A_{x'}\cos\alpha, \\ B_z &= A_{x'}\sin\alpha\sin\delta - A_{y'}\sin\alpha\cos\delta, \end{aligned} \tag{35b}$$

the normalized unit vector along the $\hat{n}\times\hat{k}$ direction can be written as

$$\hat{p} = B_x'\hat{x} + B_y'\hat{y} + B_z'\hat{z}, \tag{36}$$

where

$$B_j' = B_j/(B_x^2 + B_y^2 + B_z^2)^{1/2}, \qquad j = x, y, z. \tag{37}$$

Therefore

$$E_{in_\parallel} = E_{in}\hat{n}\cdot\hat{p} = E_{in}U_\parallel, \tag{38}$$

$$U_\parallel = u_{x'}B_x' + u_{y'}B_y' + u_{z'}B_z' \tag{39}$$

Given the incident ⊥ and ∥ field components of Eqs. (33) and (38) and the known diffraction efficiencies from Eqs. (28) and (29) for these components, the diffracted field amplitudes can be obtained as follows:

$$E_{d_\perp} = \frac{-j2\kappa}{C_d\left[\frac{\delta^2}{C_z^2} + \frac{4\kappa^2}{C_d C_z}\right]^{1/2}} \exp\left[-j\frac{\delta}{2C_z}d\right] \times \sin\left[\frac{1}{2}\left[\frac{\delta^2}{C_z^2} + \frac{4\kappa^2}{C_d C_z}\right]^{1/2} d\right] E_{in_\perp}. \quad (40)$$

$$E_{d_\parallel} = \frac{-j2\kappa|\hat{k}\cdot\hat{k}_d|}{C_d\left[\frac{\delta^2}{C_z^2} + \frac{4\kappa^2(\hat{k}\cdot\hat{k}_d)^2}{C_d C_z}\right]^{1/2}} \exp\left[-j\frac{\delta}{2C_z}d\right] \times \sin\left[\frac{1}{2}\left[\frac{\delta^2}{C_z^2} + \frac{4\kappa^2(\hat{k}\cdot\hat{k}_d)^2}{C_d C_z}\right]^{1/2} d\right] E_{in_\parallel}. \quad (41)$$

The 2-D diffraction efficiency is defined as the ratio of the real power, which is carried by the z' component of the diffracted wave, to the power associated with the corresponding component of the incident wave. The diffraction efficiency of the resultant grating-coupling process is thus given by

$$\eta = \frac{k_{dz}}{k_z}\frac{|E_{d_\perp}|^2 + |E_{d_\parallel}|^2}{|E_{in}|^2}. \quad (42)$$

We note at this point that Eqs. (40) and (41) clearly show differences in the coupling strengths for the diffracted ∥ and ⊥ field components, which are based on the $\hat{k}\cdot\hat{k}_d$ term in Eq. (41), which is in agreement with previous results.[14] Therefore it is not possible to achieve a diffraction efficiency of 100% unless the polarization of the incident field is purely a ∥ or ⊥ component in the x'–z' plane as the thickness of the grating increases.

The net electric field of the diffracted wave is obtained by the vector summation of the ∥ and ⊥ polarization components. Because of the out-of-phase couplings of the two components in the grating region, the resultant diffracted-wave polarization changes with respect to the length of propagation in the z' direction.

From the phase-matching condition and the coordinate transformation, we obtain the diffracted beam propagation constant $\mathbf{k}_d$:

$$\mathbf{k}_d = k_{dx}\hat{x} + k_{dy}\hat{y} + k_{dz}\hat{z} = (\cos\theta k_{dx} + \sin\theta\sin\beta k_{dz})\hat{x} + (\sin\theta k_{dx} - \cos\theta\sin\beta k_{dz})\hat{y} + \cos\beta k_{dz}\hat{z}. \quad (43)$$

Letting the directions of the diffracted ⊥ and ∥ components be $\hat{V}_{d_\perp}$ and $\hat{V}_{d_\parallel}$, respectively, we have

$$\hat{V}_{d_\perp} = \hat{n} = A_x'\hat{x} + A_y'\hat{y} + A_z'\hat{z}, \quad (44)$$

$$\hat{V}_{d_\parallel} = \hat{\tau} = \frac{(\hat{n}\times\mathbf{k}_d)}{|(\hat{n}\times\mathbf{k}_d)|}, \quad (45)$$

where $\hat{\tau}$ is the normalized unit vector of $(\hat{n}\times\mathbf{k}_d)$ in the diffraction plane.

Since

$$\hat{n}\times\mathbf{k}_d = C_x\hat{x} + C_y\hat{y} + C_z\hat{z} = (A_y'k_{dz} - A_z'k_{dy})\hat{x} + (A_z'k_{dx} - A_x'k_{dz})\hat{y} + (A_x'k_{dy} - A_y'k_{dx})\hat{z}, \quad (46)$$

we obtain

$$\hat{V}_{d_\parallel} = \hat{\tau} = C_x'\hat{x} + C_y'\hat{y} + C_z'\hat{z}, \quad (47)$$

where

$$C_k' = C_k/(C_x^2 + C_y^2 + C_z^2)^{1/2}, \qquad k = x, y, z. \quad (48)$$

We define the diffracted wave polarization, as shown in Fig. 2, in terms of ψ_d, the polarization angle of the diffracted beam. The α_d and δ_d as shown are given by the expressions

$$\tan\delta_d = \frac{k_{dx}}{k_{dz}}, \quad (49)$$

$$\tan\alpha_d = \frac{(k_{dx}^2 + k_{dz}^2)^{1/2}}{k_{dy}}\frac{k_{dy}}{k_{dz}}. \quad (50)$$

As for α_i, here α_d is defined to have the same sign as k_{dx}. Let $\hat{S}_{d_\perp}$ and $\hat{S}_{d_\parallel}$ be the unit vectors of $E_{d_\perp}$ and $E_{d_\parallel}$, respectively, as defined in Fig. 2. They can therefore be expressed as

$$\hat{S}_{d_\perp} = \sin\delta_d\hat{x} - \cos\delta_d\hat{y}, \quad (51)$$

$$\hat{S}_{d_\parallel} = -\cos\alpha_d\cos\delta_d\hat{x} - \cos\alpha_d\sin\delta_d\hat{y} + \sin\alpha_d\hat{z}. \quad (52)$$

Comparing the x and z components of the diffracted field in the (x, y, z) coordinate system, we obtain

$$E_{d_\perp}\sin\delta_d - E_{d_\parallel}\cos\alpha_d\cos\delta_d = E_d A_x' + E_d C_x', \quad (53)$$

$$E_{d_\parallel}\sin\alpha_d = E_d A_z' + E_d C_z'. \quad (54)$$

Therefore

$$E_{d_\parallel} = \frac{E_d A_z' + E_d C_z'}{\sin\alpha_d}, \quad (55)$$

$$E_{d_\perp} = \frac{E_d A_x' + E_d C_x'}{\sin\delta_d} + \frac{E_{d_\parallel}\cos\alpha_d\cos\delta_d}{\sin\delta_d}, \quad (56)$$

where the same complex phase term,

$$-j\exp\left[-j\frac{\delta}{2C_z}d\right],$$

in Eqs. (40) and (41) has been neglected. Keeping the diffracted field E_d positive, we define the polarization angle ψ_d as shown in Fig. 2 in the domain of [−90°, 270°] as

$$\psi_d = \begin{cases} \tan^{-1}\left|\frac{E_{d_\perp}}{E_{d_\parallel}}\right| & E_{d_\parallel} > 0 \\ 180° + \tan^{-1}\left|\frac{E_{d_\perp}}{E_{d_\parallel}}\right| & E_{d_\parallel} < 0 \end{cases} \quad (57)$$

After the diffracted wave leaves grating region, its polarization remains unchanged, since the two field components propagate in-phase within the homogeneous medium n_0.

Finally, we note that the simplified formulation of the 3-D diffraction by a holographic transmission grating as presented above can similarly be applied to the 3-D reflection hologram case, provided that appropriate modifications to the diffraction efficiency and field amplitude expressions are used.[17]

IV. Results and Discussion

Based on the simplified theoretical formulation described above, the diffraction efficiency of singly exposed holographic DCG gratings can be seen to depend not only on fundamental grating parameters but also on the polarization conditions and incident angle orientations. The diffraction efficiency dependence on the hologram thickness, the grating index modulation, the planar diffraction angle, and the angular deviation from the Bragg angle is shown in Figs. 4(a)–4(e), respectively. We note that the results in Figs. 4(c), 4 d), and 4(e) account for the diffraction from an unslanted transmission grating having an effective thickness of $2t$, since the substrate beam encounters the same grating twice as a result of the TIR at the film–air interface as shown in Fig. 1(b). This assumption is valid, provided that we neglect the difference in phase changes between TE and TM wave components incurred in the TIR process. The results in Figs. 4(a) and 4(b) consider the properties of the DCG film alone. It is well known that the protection of DCG holograms against the effects of humidity may require the use of a cover glass on top of the hologram. However, to satisfy the requirement of TIR at the film–air interface for the substrate fanout device, the use of a cover glass is not considered in the present discussion. Instead, other hermetic sealing methods, such as a glass box with dry-N_2-gas housing, may be used to protect the DCG polymer and at the same time permit TIR to occur.

In Fig. 4(a), for example, the dependence on film thickness is plotted for incident polarization angles ϕ of 0°, 30°, 60°, and 90°, respectively. Here the slant, plane of incidence, and incident wave vector angles Φ, δ, and α, respectively, have been chosen to assume the values of 90°, 30°, and 22.5°, respectively. The bulk index n_0, the index of modulation Δn, and the wavelength λ are chosen to be 1.53, 0.009, and 632.8 nm, respectively, for the calculation. As expected the efficiency varies with increasing thickness because of the different coupling strengths between the $\parallel$ and $\perp$ field components inside the grating region. This dependence is derived from the $k_z \cdot k_{gz}$ cross-product term of Eq. (4). These results are identical to those previously reported[1] and indicate that, as expected, the simplified theoretical approach reproduces the grating diffraction behavior as in the more detailed 3-D analysis. The dependence of diffraction efficiency on modulation index is shown in Fig. 4(b) for the same conditions as those used in Fig. 4(a) with the additional specification that the polarization angle and film thickness be 90° and 25 μm, respectively. The efficiency is seen to be a multivalued function that changes rapidly with increasing modulation index. It should be noted that the efficiency may not achieve a maximum of 100%, or a minimum of 0%, at some index values because of the out-of-phase coupling behavior between the $\parallel$ and $\perp$ components. However, a maximum efficiency can be obtained with a smaller Δn value by increasing either the grating thickness t or the angle β through the arrangement of angles α and δ. Furthermore, since the holographic emulsion can only accommodate a finite number of exposures at a particular modulation index Δn, the use of a smaller Δn is preferred in multiplexed holograms that require large fanout densities.

A similar trend is shown in Fig. 4(c) where efficiency is plotted as a function of planar diffraction angle ξ, a top view angle defined as $(180° - 2\delta)$, for modulation indices of 2.5, 3.5, and 4.5×10^{-3}, respectively. This planar diffraction angle is defined within the plane of the substrate and is related to the incident angle of the wave vector $\mathbf{k}$. By using the same parameters of n_0 and ϕ as in the previous two figures, with $\alpha = 50°$, $t = 50$ μm, which is twice the thicknesses used above, and $\lambda = 514.5$ nm, to be consistent with the substrate fanout experiments where an Ar-ion laser is used, the curves in Fig. 4(c) show that specific Δn values can be chosen to optimize the diffraction efficiency at a particular diffraction angle. The efficiency is seen to be much more sensitive to changes in the modulation index for the TE polarization ($\phi = 90°$, dashed curve) than for the TM polarization ($\phi = 0°$, solid curve) in the given calculation range. A strong oscillatory behavior is expected for larger Δn values, since they affect the degree of coupling of the E_{z_0} and E_{z_0} field components. The exposure parameters for multiplexed holograms can therefore be adjusted during the fabrication process to achieve a desired overall efficiency in multichannel devices. The angular selectivity $\Delta\delta$ of an unslanted grating, which is calculated for the planar diffraction angles of 30–60°, respectively, and a TM-polarized incident wave ($\phi = 0°$) with $\Delta n = 0.003$, is shown in Fig. 4(d). As expected the diffraction efficiency decreases rapidly as the angle δ is detuned away from the Bragg angle condition. In addition, an increase in the planar diffraction angle is seen to narrow the angular bandwidth of the grating by compressing the first- and second-order diffraction sidelobes and also reducing the full width at half-maximum of the central diffraction peak. A corresponding decrease in efficiency for all central and sidelobe peaks occurs as well. By using the same parameters as in Fig. 4(d), the angular selectivity $\Delta\alpha$ is calculated and plotted in Fig. 4(e). The calculated results of Figs. 4(d) and 4(e) indicate that the angular selectivity of the grating is sensitive to both changes in δ and α. Compared with the results shown later in Figs. 6–8, it is found that the angular selectivity with respect to δ is sharper than that for α at larger α, while the opposite is true

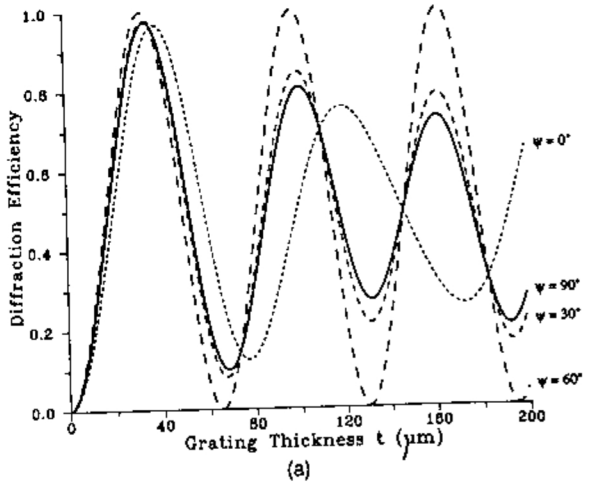

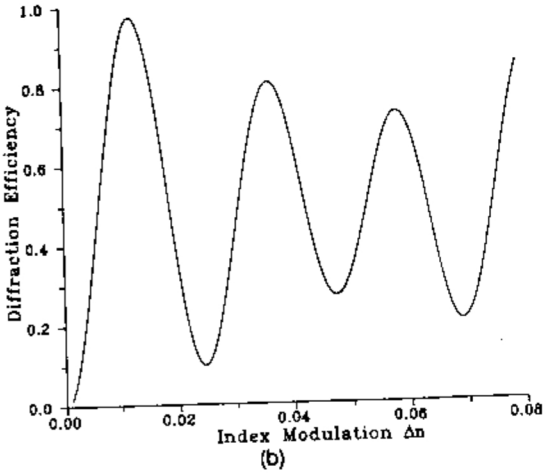

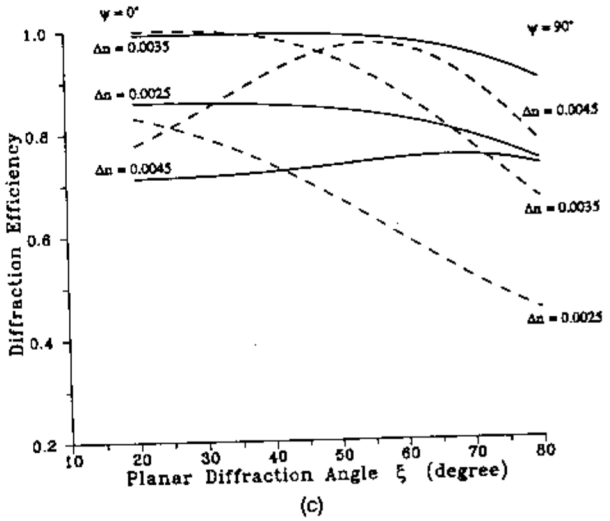

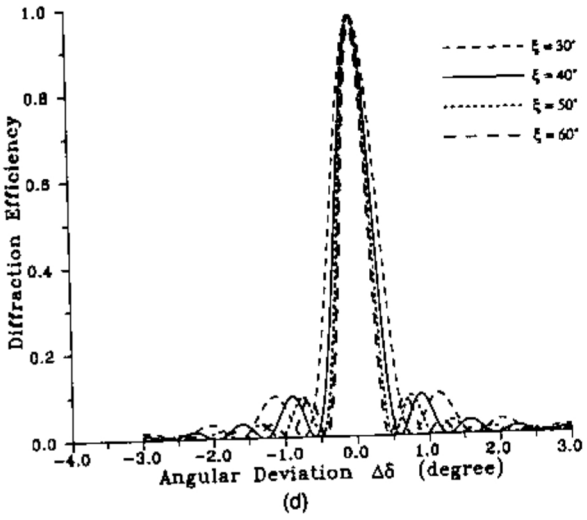

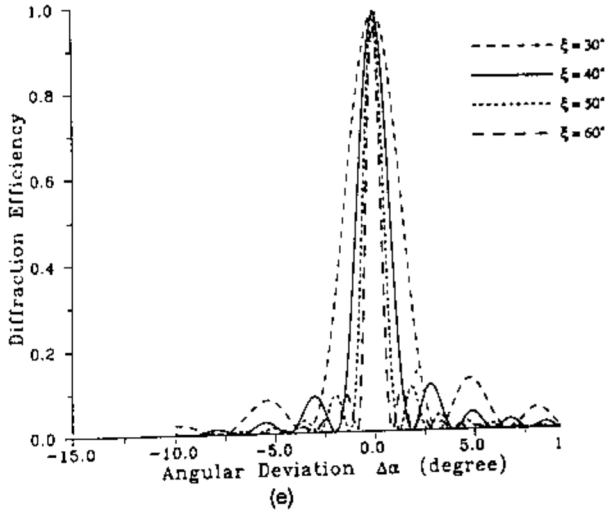

Fig. 4. Diffraction efficiency as a function of (a) the holographic film thickness, (b) the grating index modulation Δn, (c) the substrate planar diffraction angle, (d) the angular selectivity for angle δ, and (e) the angular selectivity for angle α for the substrate diffraction case. The curves in (c) are plotted for TM (solid) and TE (dashed) incident polarization, respectively.

at small α. Hence, in the case of substrate mode diffraction, as considered here, larger diffraction angles and smaller angular bandwidths should make possible higher channel densities with reduced angular overlap between adjacent channels. In addition the state of polarization of the diffracted substrate wave is shown in Fig. 5 to be a function of the planar diffraction angle and the incident polarization state. A small and continuous change in diffracted polarization angle is seen to occur for both incident TE and TM waves. Here differences in d, $k_{z'}$, $k_{dz'}$, and $\hat{k} \cdot \hat{k}_d$ values result in different diffracted $E_{d_\perp}$ and $E_{d_\parallel}$ amplitudes, respectively, at different planar diffraction angles ξ. More dramatic changes, such as polarization-switching effects, may take place at some planar diffraction angles for large grating thicknesses and

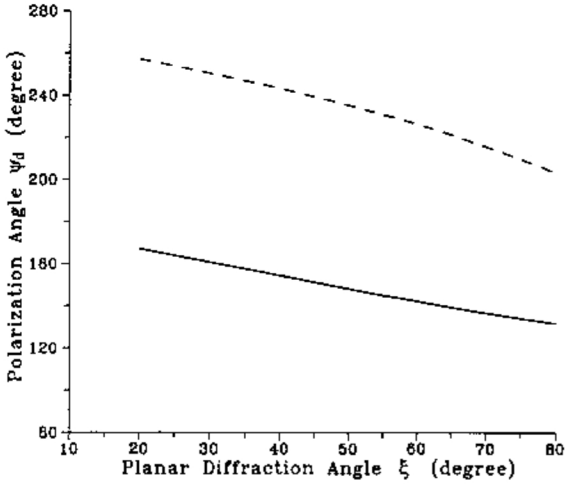

Fig. 5. Polarization angle of the diffracted substrate wave as a function of the planar diffraction angle and incident polarization state. The solid line and dashed curve are for TM ($\psi = 0°$) and TE ($\psi = 90°$) polarizations, respectively.

index modulation values. Variations in the output channel polarization state can therefore be expected and should be accounted for in the design of optical interconnects.

The following conclusions can therefore be drawn from the theoretical results of Section III. First, based on the selection of grating thickness and modulation index, a maximum diffraction efficiency of 100% can be achieved for purely $\parallel$ or $\perp$ incident field components, while other polarization orientations yield efficiencies that are significantly less than this maximum value. Second, the angle δ yields an angular selectivity that is narrower and sharper than that of α at a large incident angle and is therefore an important design parameter in multiplexed holographic grating systems. Last, the diffraction efficiency for each planar diffraction angle ξ or plane of incidence angle δ can be optimized by controlling the modulation index during the grating recording process.

To confirm the above results DCG thick holographic grating samples[18–21] were prepared on top of a soda-lime glass substrate. After spin coating the substrate with DCG films, the films were dried and stabilized in a temperature and humidity-controlled environment. Single holographic grating patterns were then recorded by using a two-beam interference method at the Ar^+ laser wavelength of 514.5 nm and were subsequently processed by using a standard fix, water rinse, and alcohol bath dehydration process. Even though the interference fringe slant angles were designed to be nearly 90°, we note that some fringe bending can occur during the film hydration and dehydration process. This effect, however, was considered to be negligible in the present set of experiments. The refractive index of the resulting film was measured by treating the DCG film as a thick optical waveguide and by using a prism-coupling technique to couple to the fundamental mode of the slab guide. The effective index of the mode, which can be used to approximate the bulk index of the multimode film, was found to be ~1.53. The thickness of the recorded hologram was measured to be ~23.6 μm. We note that, unlike other holograms, such as holographic lens elements, which consist of many local Bragg gratings of different grating amplitudes and orientations, the singly recorded phase gratings of grating vector **K** are made to satisfy the Bragg condition at different reconstruction wavelengths, $K = 2k_0 \sin \theta_B$, through angular alignment of the incident reconstruction beam. Here k_0 is the reconstruction beam propagation constant in the medium of index n_0 and θ_B is the Bragg diffraction angle that is a function of α and δ in the present case. For example, diffraction from an unslanted phase grating ($\phi = 90°$) with $\delta = 0°$ incidence produces $\theta_B = \alpha = \alpha_d$ as shown in Fig. 2. The grating is recorded with a similar geometry as in the reconstruction but with different k_0 and θ_B. Holographic elements, other than multiplexed transmission gratings, that are reconstructed at wavelengths other than their original recording wavelength often suffer aberration effects and reduced efficiencies. This point is addressed later.

Efficiency measurements were made by mounting the grating samples on a goniometer stage that could vary both the in-plane rotation angle δ and the incident beam angle α. A collimated light beam from a 632.8-nm He–Ne laser, a wavelength that is different from the recording wavelength, was polarized by using a Glan–Taylor prism, which is projected onto the sample and collected from both the diffracted and undiffracted beams. Efficiencies were then measured as a function of α, δ, and incident beam polarization angle ψ. Fresnel reflection losses from the air–glass and air–film boundaries were neglected in the efficiency calculations, since both the diffracted and undiffracted beams experience the same percentage of reflection loss. Angular sensitivity measurements were made by fixing two of the above angles and varying the third angle around the peak of the respective diffraction angle. The results of α- and δ-dependent measurements for 2-D ($\delta = 0°$) and 3-D ($\delta \neq 0°$) single-grating diffraction as a function of the incident polarization angle and their comparison with the theoretical results of Section III are shown in Figs. 6–8, respectively.

In Fig. 6 the diffraction efficiency is shown as a function of incident angle α for the polarization angles of 0°, 60°, and 90°, respectively. The base line for the curves, which is offset for clarity, is indicated by dashed lines in Fig. 6. Here $\delta = 0°$ and the plane of incidence is coincident with the plane that contains the grating wave vector. The index modulation parameter Δn is the only adjustable parameter that is used in the curve fitting process. In this case a modulation index of 9.8×10^{-3} was used to provide a consistent fit for all three polarization conditions. Its value is in fact much larger than that normally used in the case of multiplexed gratings for substrate mode diffraction. The experimental and theoretical results correlate well, both in predicting the peak diffraction

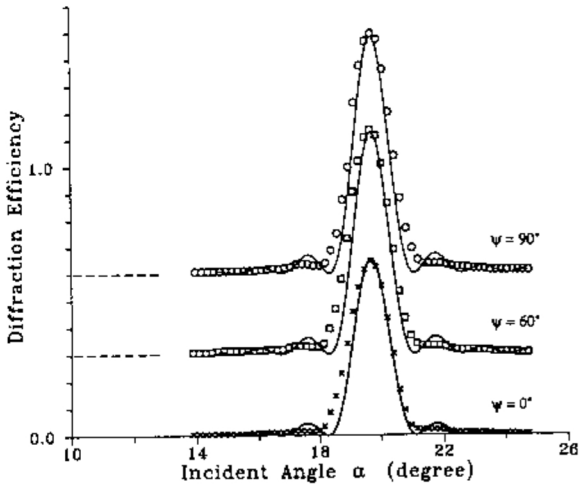

Fig. 6. Grating response as a function of the incident angle α for the 2-D diffraction ($\delta = 0°$) and the polarization angle ψ of 0°, 60°, and 90°, respectively. The curves are calculated by using the following values: $t = 23.6$ μm, $n = 1.53$, $\Delta n = 9.8 \times 10^{-3}$, and $\lambda = 632.8$ nm. Symbols represent experimentally measured data points.

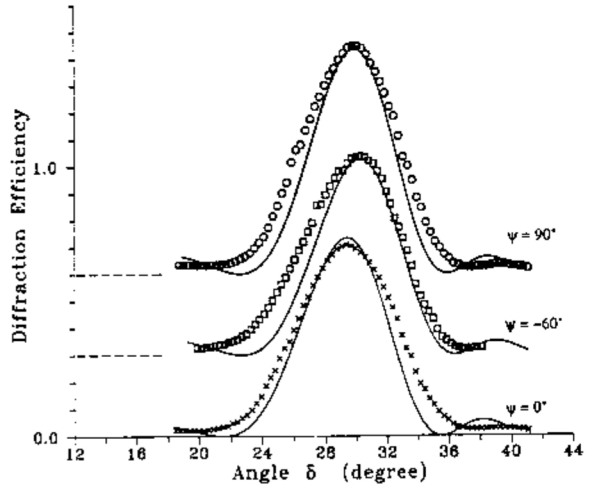

Fig. 8. Parametric dependence of the diffraction efficiency on the in-plane rotation angle δ that is measured for the polarization angles ψ of 0°, −60°, and 90°, respectively.

efficiency and in the angular bandwidth (full width at half-maximum). The peak efficiency is seen to decrease with the change in the incident polarization angle from 90° (TE) to 0° (TM) for the present device. This trend may be different for other devices with different grating parameters. All other features, however, remain essentially unchanged. The measured angular bandwidths are slightly larger than the calculated results and may be caused by variations in the modulation index inside the film caused by film hydration and dehydration during the hologram processing procedure. Such variations could produce a smaller effective grating interaction length and hence a wider angular bandwidth. If, for example, a film thickness of 22 μm is used in the data fits, instead of the measured value of 23.6 μm, a nearly perfect fit can be achieved. The relatively poor fits of the first- and second-order diffraction sidelobes and the lack of distinct sidelobe minima are believed to be caused by this same depth profiling effect within the film. Finite beam effects, not accounted for in the present treatment, could also represent another possible source of error.

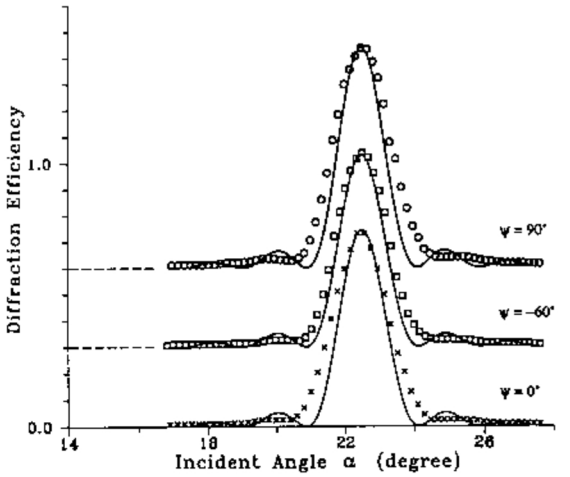

Fig. 7. Grating response for 3-D diffraction ($\delta = 30°$) as a function of the incident angle α for the polarization angles ψ of 0°, −60°, and 90°, respectively. All other parameters are the same as those in Fig. 6.

Similar results are seen in the 3-D diffraction data of Fig. 7. Here $\delta = 30°$, and ψ assumes the values of 90°, −60°, and 0°, respectively. The same modulation index is seen to fit the peak efficiencies well, while the angular bandwidths exhibit slightly larger deviations. These results are also reflected in the response plots of Fig. 8, where the efficiency is plotted as a function of angular variations in δ for an angle $\alpha = 22.7°$. Once again a systematic decrease in peak efficiency is observed as the polarization angle ψ is rotated from 90° to 0° for the present device. The shift in the TM curve ($\psi = 0°$) to a smaller δ by ~0.92° in Fig. 8 is likely to be due to an experimental deviation in δ, as measured on the goniometer stage.

V. Use of Multiplexed Holograms for Multiplanar Substrate Interconnection

The above results on thick DCG holographic singly exposed gratings can be used to optimize the behavior of multiplexed gratings, which are exposed successively in the same holographic emulsion, for optical interconnection applications that require large fanout densities and negligible channel cross talk. By using multiplexed holograms in conjunction with substrate wave propagation, we show below that it is possible to achieve fanout densities of up to 1 × 30 with good overall diffraction efficiencies.

The multiplexed holographic gratings considered here are formed by sequentially recording single gratings that have been designed for operation at a specific Bragg diffraction angle. Each individual holographic grating is recorded so that

$$K_i = 2k_\parallel \sin\left(\frac{\xi}{2}\right), \tag{58}$$

where $k\|$ and K_i are defined as

$$k_{\|} = \frac{2\pi}{\lambda} n \sin \gamma, \tag{59}$$

$$K_i = \frac{2\pi}{\Lambda_i}. \tag{60}$$

Here $k\|$ is the horizontal component of the substrate mode propagation constant, K_i and Λ_i are the wave vector and period of the ith holographic grating, respectively, ξ_i is the diffraction angle for the ith diffracted beam within the grating plane, n is the substrate refractive index, γ is the substrate mode bouncing angle, which is measured with respect to the substrate normal, and λ is the free-space wavelength. The γ and n are related to the incident angle α and grating bulk index n_0 by the Fresnel refraction equation. In the present case the refractive index of the soda-lime glass substrate ($n = 1.51$) is close to the bulk index of holographically exposed DCG film ($n_0 \approx 1.53$). Hence the angle γ and α are nearly identical, and the reflection at the substrate–film interface can be ignored.

From Fig. 4(c) we recall that the diffraction efficiency depends not only on the planar diffraction angle but also on the magnitude of the grating modulation index. To achieve a high diffraction efficiency for each channel in a multiplexed system, the exposure parameters and hence the modulation index must be optimized during the recording process. DCG is known to have a maximum modulation index of ~0.1 (Ref. 18) before the index response saturates with the increasing exposure dosage. For a film thickness of ~25 μm and an estimated average index modulation $\Delta n_{av} = 2.5 \times 10^{-3}$/exposure, this permits a maximum of ~40 fanout channels to be defined in the DCG film at the given bouncing angle. The number of multiplexed channels can be increased by increasing the film thickness by increasing the angle β through the choice of angles α and δ or by lowering the efficiency requirement for each channel, which in turn reduces the magnitude of the required Δn_{av}.

An example of combining holographic grating elements with substrate wave propagation for the optical interconnection is shown in Fig. 9. Here an ~25-μm-thick DCG film that contains a singly exposed phase grating has been patterned on top of a soda-lime glass substrate, as described previously. A substrate mode that is excited by prism coupling can be seen propagating by means of TIR between the upper and lower surfaces of the substrate. On its encounter with the phase grating on the upper surface, the mode is diffracted at the designed Bragg angle. Two different grating samples show planar diffraction at angles of 55° and 70° in Figs. 9(a) and 9(b), respectively. A portion of the incident beam remains undiffracted and continues to propagate through the substrate. Diffraction efficiencies of 90% at 40°, 88% at 55°, and 84% at 70° have been experimentally measured for three samples and compare favorably with the calculated maximum theoretically achievable efficiency values of 99.7, 98.5, and 94.7%, respectively, by using an incident beam polarization of $\psi = 0°$ and a bouncing angle $\alpha = 50°$ at a 514.5-nm wavelength. We note that 100% efficiency cannot be achieved in the case of a lossless grating because of the out-of-phase coupling that occurs between the $\|$ and $\perp$ field components for a TM-polarized incident mode.

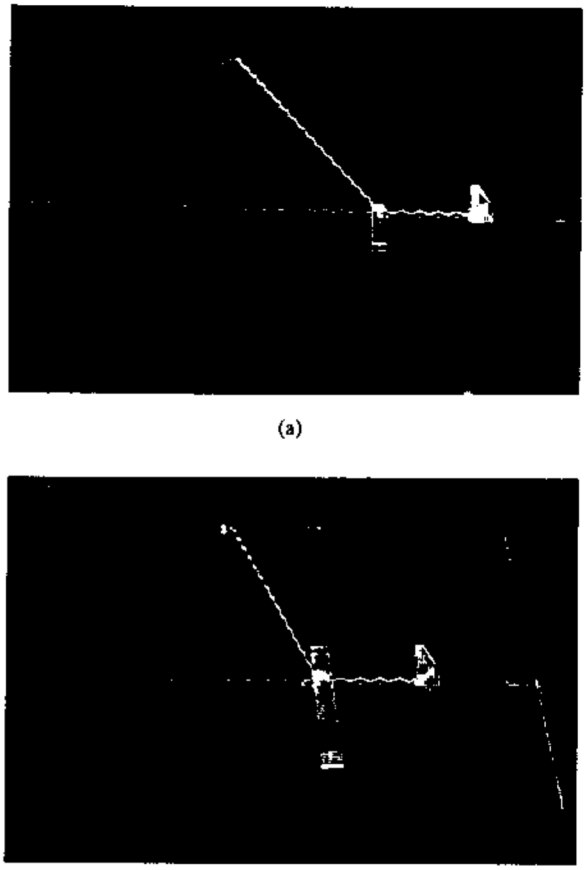

(a)

(b)

Fig. 9. Substrate diffraction from singly exposed DCG phase gratings at angles of (a) 55° and (b) 70°, respectively. The mode propagation within the glass substrate is seen to produce zigzag ray paths as the light bounces between the upper and lower substrate surfaces.

When holographic gratings are multiplexed, large fanout densities can be achieved with the substrate propagation technique. An example of a 1-to-30 substrate optical fanout, which operates at 514.5-nm, is shown in the substrate top view of Fig. 10. Successive holographic recordings were used to produce 30 separate diffraction channels over a range of planar diffraction angles from 30° to 88° with a 2° angular separation between adjacent channels. The corresponding efficiency plot, presented in Fig. 11 for an incident polarization angle $\psi = 0°$, shows that the individual channel efficiencies are ~3.0 ± 0.8%, while the overall device efficiency, which is obtained by summing up the individual channel responses, is nearly 87.8%. The fanouts at the smallest and largest diffraction angles are seen to produce the lowest efficiencies. These differences may result from varia-

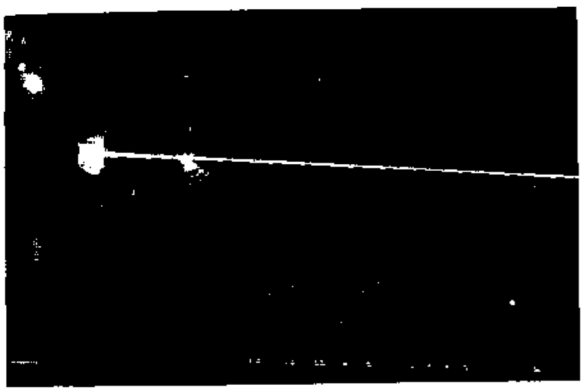

Fig. 10. A 1-to-30 fanout optical interconnect operating at 514.5 nm by using multiplexed Bragg gratings and substrate propagation. The device exhibits an overall efficiency of ~87.8%.

tions in recording dosages that are derived from power fluctuations and invalid predictions that use single-grating diffraction theory. Compared with the single-grating results of Fig. 4(c), in the case where all gratings are assumed to be exposed in the same conditions and each grating has a $\Delta n_{av} \cong 2.5 \times 10^{-3}$, the measured and calculated results follow a similar trend at high planar diffraction angles only. The multiple grating shows a more complicated angular dependence that cannot be explained by the present theoretical analysis. However, the depolarization effects caused by the mutual coupling between all gratings are believed to be one source for error and require further study. Here variations in efficiency as a function of planar diffraction angle are expected unless exposure parameters and the resulting modulation indices are optimized for each channel to be defined. By using the above parameters the angular and wavelength selectivities for single-grating substrate diffraction, as it is applied to our 1-to-30 fanout device, can be estimated. These results are shown in Table I and may in part describe the performance of our large fanout optical interconnect. In general, both

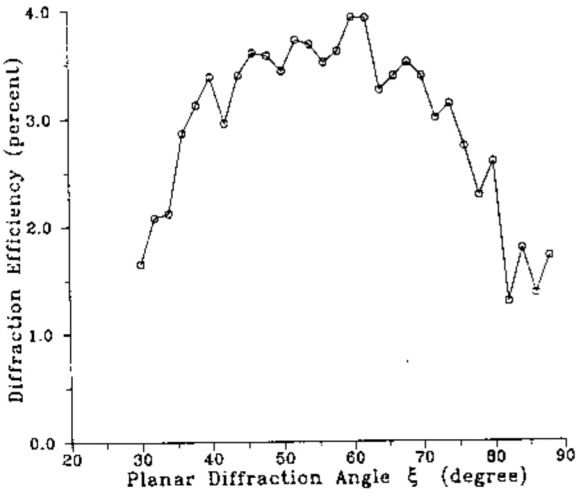

Fig. 11. Diffraction efficiency as a function of the substrate planar diffraction angle for the 1-to-30 fanout interconnect of Fig. 10. The average efficiency per channel is ~3.0%.

Table I. Angular and Wavelength Selectivity of Singly Exposed Gratings That are Used to Construct a 1-to-30 Fanout Optical Interconnect at 514.5 nm

Planar Diffraction Angle ξ (deg)	Angular Bandwidth Δξ (deg)	Spectral Bandwidth Δλ (nm)
30	1.30	22.5
50	0.90	8.4
70	0.72	4.6
80	0.70	3.7

the angular and spectral bandwidths decrease as the planar substrate diffraction angle increases. The full width at half-maximum spectral bandwidth is seen to experience the greatest variation, decreasing from 22.5 nm at 30° to 3.7 nm at 80°. Although not explicitly expressed in the efficiency expressions of Eqs. (40)–(42), the planar diffraction angle ξ is related to the angle δ by (180° − 2δ), while the wavelength λ is related to both the wave propagation constant k_0 and the coupling constant κ. For a fixed incident angle α and grating vector **K**, variations in the angle ξ or wavelength λ undoubtedly affect the incident **k** direction or its amplitude through Eq. (4b) and in turn cause the phase matching to deviate from the Bragg condition. The contribution from the coupling constant κ is negligible for small λ variations. Improvement in both angular and spectral selectivities at a larger diffraction angle can be achieved with a larger grating constant K as shown in the following equation, which is derived from the phase-matching condition in Fig. 3. A negative value of α′ in Fig. 3 has been taken into account in the derivation. Hence

$$\vartheta = \frac{k_0^2 - k_d^2}{2k_0} \approx -\frac{K^2}{4\pi n_0}\lambda \mp K\cos(\phi' - \alpha') \qquad \phi' - \alpha' > 90°\ (<90°). \tag{61}$$

From Eq. (61) it can be seen that a larger K value makes k_d more sensitive to variations in λ. The corresponding efficiency is changed through the dephasing constant ϑ. The trend of a decreasing bandwidth with an increasing diffraction angle is consistent with 2-D calculations on WDM devices.[21] A smaller dependence of angular bandwidth on angle ξ may result from the complicated and indirect relationship between α′, φ′, and ξ. The design of efficient large fanout optical interconnects[22] based on multiplexed gratings and substrate propagation must therefore take into account the complex interdependence between grating parameters, incident and diffracted polarization states, fanout density, and fanout direction, as described above.

Based on the above analysis that demonstrates that excellent wavelength selectivities can be achieved at large planar diffraction angles ξ, it should be possible to multiplex multiple gratings for different sources to form a wavelength division multiplexing device in the substrate configuration. Each grating in the multiplexed system is designed to diffract selectively one

incoming signal carrier wavelength in the Bragg regime. Hence a signal carrier wavelength λ_i is to be Bragg diffracted only by grating $\mathbf{K}_i$. However, because of the presence of other gratings, it is possible that the same signal carrier will experience both diffractions and reflections with low efficiencies at the film–air interface by these gratings. These diffracted beams, which have different bouncing angles and planar diffraction angles, may not overlap with other Bragg diffracted signals. Thus with proper design it should be possible to achieve low cross talk for a substrate wavelength division multiplexing system.

The present measurement of diffraction efficiency was performed by dividing the power in the diffracted beam by the sum of the powers in the undiffracted and diffracted beams. The absorption and scattering in the hologram can be characterized as hologram excess loss L_a that is measured to be approximately −0.5 dB. The absorption and scattering in glass, and the reflection loss at the air–glass boundaries, can be characterized as substrate wave propagation loss L_p and is estimated at less than −0.5 dB/cm. In the Bragg regime power diffracted into other diffracted orders can be neglected, except in the wavelength division multiplexing case where additional diffraction loss needs to be considered. Other system losses, which result from beam collimation and focusing, can be characterized as L_s. The values of L_s may vary within a few decibels and depend on the quality and alignment of these holographic optical elements. These losses, along with coupling losses L_c of approximately −2 dB, from laser to substrate wave and from focused beam to detector, were not considered in the efficiency determination but are considered separately. All of them are important for the determination of the power budget requirement for substrate interconnect systems.

Refinements in multichannel processing techniques should make possible better uniformity and higher channel densities in multiplexed systems that utilize the substrate, and the reflections from its surfaces, for high-density optical interconnection. The design and fabrication of high efficiency and low aberration collimation and focusing elements[13,14] for the substrate waves present other challenging issues that need to be considered in interconnect systems. The aberration problems can be corrected by recording the holographic optical elements with aspheric wave fronts derived from other aberration correcting holographic optical elements. Further theoretical work is also needed to account for the simultaneous interaction between the incident beam and all multiplexed gratings and its effect on the angular selectivity and spectral bandwidth of the system.

VI. Conclusions

A large fanout optical interconnection scheme that utilizes the diffraction from thick holographic DCG gratings and substrate wave propagation has been described. Based on the above scheme, a 1-to-30 fanout device, which exhibits excellent overall diffraction efficiency, has been demonstrated. Here the large fanout density is produced by multiplexing single-diffraction-order Bragg gratings rather than multiple-order gratings. Such a device should find wide application in systems that require the high-speed optical interconnection of very large-scale integrated circuits, wafer-scale integrated circuits, or even optoelectronic integrated circuits that reside on the same, or different, optical planes of a common substrate.

Experiments on single and multiplexed gratings indicate that diffraction efficiencies and angular bandwidths correlate well with calculated results. The parametric relationship between the grating modulation index, interaction length, Bragg diffraction angle, and diffraction efficiency is well understood and can be predicted by using a simplified theoretical formulation that reduces the general 3-D diffraction problem into a more tangible 2-D problem in the Bragg regime. The realization of even higher fanout density optical interconnects by using the substrate wave propagation technique should be possible.

This research project is currently sponsored by Defense Advanced Research Project Agency contract DAAH01-89-C-0164.

References

1. J. W. Goodman, F. J. Leonberger, S. Y. Kung, and R. A. Athale, "Optical interconnections for VLSI systems," Proc. IEEE **72**, 850–866 (1984).
2. I. D. Hutcheson, "High speed optical interconnects for computing applications," in *Optical Interconnections*, G. C. Righini and O. D. Soares, eds., Proc. Soc. Photo-Opt. Instrum. Eng. **862**, 2–10 (1987).
3. M. R. Feldman, S. C. Esener, C. C. Guest, and S. H. Lee, "Comparison between optical and electrical interconnects based on power and speed considerations," Appl. Opt. **27**, 1742–1751 (1988).
4. L. A. Bergman, W. H. Wu, A. R. Johnston, R. Nixon, S. C. Esener, C. C. Guest, P. Yu, T. J. Drabik, M. Feldman, and S. H. Lee, "Holographic optical interconnects for VLSI," Opt. Eng. **25**, 1109–1118 (1986).
5. M. R. Feldman and C. C. Guest, "Computer generated holographic optical elements for optical interconnection of very large scale integrated circuits," Appl. Opt. **26**, 4377–4384 (1987).
6. R. K. Kostuk, J. W. Goodman, and L. Hesselink, "Optical imaging applied to microelectronic chip-to-chip interconnections," Appl. Opt. **24**, 2851–2858 (1985).
7. K. H. Brenner and F. Sauer, "Diffractive-reflective optical interconnects," Appl. Opt. **27**, 4251–4254 (1988).
8. J. Jahns and A. Huang, "Planar integration of free-space optical components," Appl. Opt. **28**, 1602–1605 (1989).
9. R. K. Kostuk, Y. T. Huang, D. Hetherington, and M. Kato, "Reducing alignment and chromatic sensitivity of holographic optical interconnects with substrate-mode holograms," Appl. Opt. **28**, 4939–4944 (1989).
10. R. T. Chen, M. R. Wang, and T. Jannson, "Intra plane guided wave massive fanout optical interconnects," Appl. Phys. Lett. **57**, 2071–2073 (1990).
11. F. Liu, E. Strzelecki, and T. Jannson, "Optical multiplanar VLSI interconnects based on multiplexed waveguide holograms," Appl. Opt. **29**, 1126–1133 (1990).
12. J. L. Jewell, Y. H. Lee, A. Scherer, S. L. McCall, N. A. Olsson, J. P. Harbison, and L. T. Florez, "Surface-emitting microlas

ers for photonic switching and interchip connections," Opt. Eng. **29**, 210–214 (1990).
13. E. Yablonovitch, D. M. Hwang, T. J. Gmitter, L. T. Florez, and J. P. Harbison, "Van der Waals bonding of GaAs epitaxial liftoff films onto arbitrary substrates," Appl. Phys. Lett. **56**, 2419–2421 (1990).
14. M. G. Muharam and T. K. Gaylord, "Three-dimensional vector coupled-wave analysis of planar-grating diffraction," J. Opt. Soc. Am. **73**, 1105–1112 (1983).
15. M. G. Muharam and T. K. Gaylord, "Rigorous coupled-wave analysis of planar-grating diffraction," J. Opt. Soc. Am. **71**, 811–818 (1981).
16. M. G. Moharam and T. K. Gaylord, "Rigorous coupled-wave analysis of grating diffraction: E-mode polarization and losses," J. Opt. Soc. Am. **73**, 451–455 (1983).
17. H. Kogelnik, "Coupled wave theory for thick hologram gratings," Bell Syst. Tech. J. **48**, 2909–2947 (1969).
18. D. Meyerhofer, "Achromated gelatin," in *Holographic Recording Materials*, H. M. Smith, ed., Vol. 20 of Topics in Applied Physics (Springer-Verlag, Berlin, 1977), 75–99.
19. B. J. Chang and C. D. Leonard, "Dichromated gelatin for the fabrication of holographic optical elements," Appl. Opt. **18**, 2407–2417 (1979).
20. R. T. Chen, W. Phillips, T. Jannson, and D. Pelka, "Integration of holographic optical elements with polymer gelatin waveguides on GaAs, $LiNbO_3$, glass, and aluminum," Opt. Lett. **14**, 892–894 (1989).
21. M. R. Wang, R. T. Chen, G. J. Sonek, and T. Jannson, "Wavelength division multiplexing and demultiplexing in locally sensitized single-mode polymer microstructure waveguides," Opt. Lett. **15**, 363–365 (1990).
22. R. T. Chen, "Optical interconnects: a solution to very high speed integrated circuits," in *Integrated Optics and Optoelectronics II*, K. Wong, ed., Proc. Soc. Photo-Opt. Instrum. Eng. **1374**, 20–32 (1990).
23. K. Winick, "Designing efficient aberration-free holographic lenses in the presence of a construction-reconstruction wavelength shift," J. Opt. Soc. Am. **72**, 143–148 (1982).
24. M. Assenheimer, Y. Amitai, and A. A. Friesem, "Recursive design for an efficient HOE with different recording and readout wavelengths," Appl. Opt. **27**, 4747–4753 (1988).